Available online at www.sciencedirect.com
ScienceDirect
Trans. Nonferrous Met. Soc. China 33(2023) 1305−1317
Transactions of Nonferrous Metals Society of China
www.tnmsc.cn

Investigation of precipitation strengthening behavior of Al−Mg−Si alloy using SAXS

Tao LIU[1,2,3], Guang-min HU[1], Yu-jie WANG[1], Jian-rong ZENG[2,3], Qing DONG[1], Feng-gang BIAN[2,3], Zhao-peng CAO[2,3], Nan MENG[2,3], Jiao ZHANG[1,4,5], Bao-de SUN[1,4,5]

1. Shanghai Key Lab of Advanced High-temperature Materials and Precision Forming, School of Materials Science and Engineering, Shanghai Jiao Tong University, Shanghai 200240, China;
2. Shanghai Advanced Research Institute, Chinese Academy of Sciences, Shanghai 201204, China;
3. Shanghai Institute of Applied Physics, Chinese Academy of Sciences, Shanghai 201800, China;
4. State Key Lab of Metal Matrix Composites, Shanghai Jiao Tong University, Shanghai 200240, China;
5. Collaborative Innovation Center for Advanced Ship and Deep-sea Exploration, Shanghai Jiao Tong University, Shanghai 200240, China

Received 16 November 2021; accepted 20 April 2022

Abstract: The precipitation strengthening behavior and its effect on mechanical properties of Al−Mg−Si alloy during isothermal aging were investigated. In-situ synchrotron small angle X-ray scattering (SAXS) technique was used to characterize the nanoprecipitates and their structural parameters (size, volume fraction and number density) combined with transmission electron microscopy (TEM). The results show that rod-shaped β'' precipitates grow preferentially along their longitudinal dimensions, but the radial dimension reaches a plateau after 5 h of aging. The growth of nanoprecipitates in size and volume fraction is quantitatively related to precipitation strengthening, as shown by predictions and measurements of relevant yield strength and hardness. SAXS provides more reliable input parameters for the Ashby−Orowan model, which improves the predictive accuracy and generalizability of the model. The study demonstrates that with increasing the aging time, the evolution of predictive mechanical properties of Al−Mg−Si alloy is dependent on the mean radius and volume fraction of β'' precipitates.

Key words: precipitation behavior; Al−Mg−Si alloy; small angle X-ray scattering; mechanical properties

1 Introduction

Al−Mg−Si alloys (6xxx series) are widely used in the automotive industry because of their high specific strength, good formability and corrosion resistance [1,2]. Al−Mg−Si alloys are strengthened by forming nanoprecipitates (β'' and β' [3,4]) during the aging process. Since precipitation strengthening plays a dominant role in the strengthening mechanism of aluminum alloys, predicting the mechanical properties based on precipitate evolution has been one of the research hotspots. Therefore, it is of great scientific and technological significance to characterize the nanoprecipitates structure of Al−Mg−Si alloys and uncover the relationship between micro-structure and mechanical properties by combining experimental measurement and performance model prediction.

Abundant studies using the differential scanning calorimetry (DSC) [5,6], the transmission electron

Corresponding author: Jian-rong ZENG, Tel: +86-21-20304853, E-mail: zengjianrong@sinap.ac.cn;
Qing DONG, Tel: +86-15901904159, E-mail: dqmail@sjtu.edu.cn
DOI: 10.1016/S1003-6326(23)66184-9

microscopy (TEM) [7−9], and the atom probe tomography (APT) [10−12] have been implemented to measure the size, composition and morphology of nanostructures of β'' precipitates in Al−Mg−Si alloys. However, these conventional methods are limitedly capable of acquiring statistical data on numerous precipitates, restricting the application and development of performance prediction models due to a lack of accuracy and reliability. For example, the Ashby−Orowan model [13] is broadly applied in steel [14,15], aluminum alloy [16−18] and magnesium alloy [19,20] as an effective precipitation strengthening model, aiming to link the model-predicted strength with experimental performance. Nevertheless, the predicted yield strength of aluminum alloy using the Ashby−Orowan model with TEM characterization still has a relatively high error [21−23]. Therefore, it is crucial to characterize with statistical significance on structure parameters such as the size and volume fraction of numerous nanoprecipitates in bulk samples.

The small angle X-ray scattering (SAXS) technique [24,25] is potentially suitable for statistically characterizing β'' precipitates of Al−Mg−Si alloys because of its in-situ detection, non-destructive sample preparation and good statistics. SINGH et al [26] studied deformation-induced nanovoids in AA6063 aluminum alloy. They found that the measured void volume fraction using SAXS is consistent with model predictions of the volume fraction of vacancies during plastic deformation. BANHART et al [27] investigated the clusters of Al−Mg−Si using in-situ SAXS measurements and revealed the structure of Si or Cu containing clusters when it is performed near the Si K-edge (1.84 keV) or Cu K-edge (8.98 keV). It is notoriously difficult to perform such applications on Al−Mg−Si alloy due to the very low electron density contrast between β'' precipitates and Al matrix, resulting in the fact that few relevant publications can be accessed [28−30]. However, to the best of our knowledge, the relationship between precipitate structural evolution and strengthening behavior of Al−Mg−Si alloys using in-situ SAXS combined with the strengthening model has not been reported to date.

This study aims to use in-situ SAXS to quantitatively and statistically characterize the structural parameters of precipitates and investigate the precipitation strengthening behavior. We utilized precipitate radius and volume fraction as input parameters of the Ashby−Orowan model and predict mechanical properties of Al−Mg−Si alloy. Furthermore, the results will aid in modeling precipitation strengthening and selecting proper heat treatment processing schedules for controlled nanoprecipitate with a SAXS methodology, extending to a broader range of aluminum alloys.

2 Experimental

2.1 Sample preparation

The composition of Al−Mg−Si (6082) alloy analyzed by inductively coupled plasma-optical emission spectroscopy (ICP-OES) was Al−1.01Mg−0.89Si−0.14Cr−0.13Fe (wt.%). The schemes of the hot treatment process are shown in Fig. 1(a). Firstly, the billets with dimensions of d180 mm × 200 mm were homogenized at 560 °C for 6 h, followed by

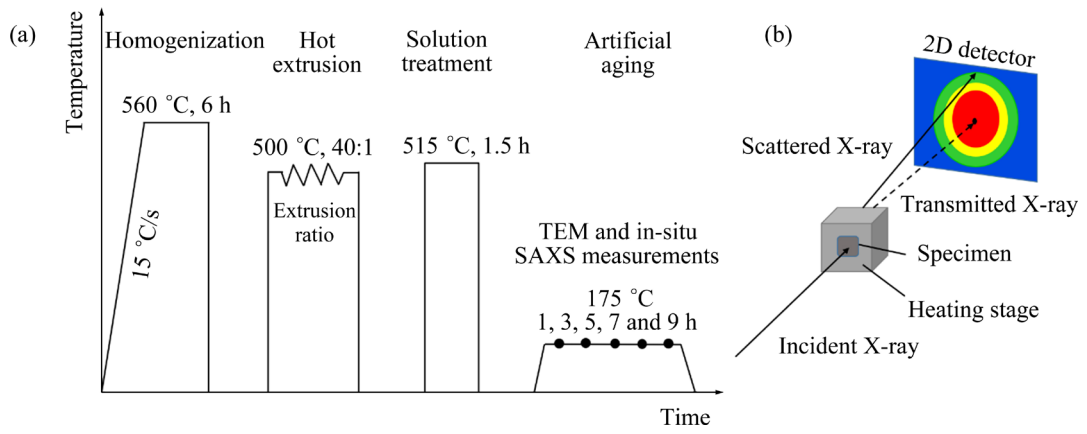

Fig. 1 Schemes of heat-treatment process during in-situ SAXS measurement (a) and in-situ SAXS experimental devices (b)

water cooling. The heating rate applied was 15 °C/s. Subsequently, the hot extrusion was carried out at 450 °C with an extrusion ratio of 40:1 and a speed of 1 mm/s. Additionally, the samples were solution-treated at 515 °C for 1.5 h, quenched in water, and then artificially aged at 175 °C for 1, 3, 5, 7, and 9 h, respectively. Three ex-situ specimens (1, 5 and 9 h) were prepared for investigation using TEM.

2.2 SAXS experiments

The in-situ synchrotron SAXS measurements were performed in transmission mode at beamline BL16B1, Shanghai Synchrotron Radiation Facility (SSRF) in China. The schematic diagram of the SAXS experimental devices is presented in Fig. 1(b). The monochromatic beam (incident X-ray) of 10 keV photons was irradiated on the aged sample foil with a thickness of 80 μm. The two-dimensional (2D) charge-coupled device detector (Rayonix SX165) was conducted to collect SAXS signals with a sample-to-detector distance of 1840 cm. Then, the solution-treated specimen was fixed inside a program-controlled heating stage (Linkam THM600) and was heated to an artificial aging temperature of 175 °C with a heating rate of 10 °C/min. The SAXS data were collected every 120 min with an exposure time of 100 s during isothermal aging. Particularly, the SAXS data were calibrated and converted to absolute units by measuring the glassy carbon standard sample. The 2D SAXS patterns were reduced into 1D SAXS curves in terms of scattering vector using the Fit2d software. Quantitative precipitates microstructural parameters were acquired by model simulation using a self-made MATLAB program.

2.3 Microstructure characterization and mechanical properties

TEM analyses were performed employing a JEM−2100F instrument operated at 200 kV. The TEM foils were electropolished by a twinjet machine with 25% nitric acid solution in methanol at −25 °C and 20 V. Analysis of TEM images was conducted by the Gatan Digital Micrograph™ software. The quantitative microstructural characterization was realized using the ImageJ software. The mean size of precipitates can be acquired from equivalent circle diameter (D_{EC}) $D_{EC}=2\sqrt{A/\pi}$ and mean diameter (D_m) $D_m=P/\pi$, where A is the precipitate area and P is the precipitate perimeter. The tensile properties at room temperature were carried out by a BTC-T1-FR020 test machine at an identical rate of 1 mm/min.

3 Precipitation strengthening model

3.1 Microstructure description

The precipitate radius and length vary with aging time, and the expressions of radius (r) and length (l) for rod-like precipitates β'' can be expressed as [31]

$$r=\frac{2}{3}\sqrt{\alpha Dt} \tag{1}$$

$$l=\frac{2}{3}\sqrt{A_1^2\alpha Dt} \tag{2}$$

where A_1 is the aspect ratio of precipitates, D is the diffusion coefficient, t is aging time, and α is a dimensionless growth parameter which can be expressed as [32]

$$\alpha=\left(\frac{C_0-C_e}{C_p-C_e}\right)/\left(pA_1\right) \tag{3}$$

where C_0 is the average solute content of magnesium in the matrix with mass fraction, C_e is the equilibrium solute content at the particle/matrix interface (obtained by phase diagram), and C_p is the solute concentration of precipitate. p is a factor, of which 2/3 is taken to express the effect of continuous precipitation [31]. Diffusion coefficient (D) has an Arrhenius-type relationship with the thermodynamic temperature (T):

$$D=D_0\exp[-Q_d/(RT)] \tag{4}$$

where D_0 is the pre-exponential term for D, Q_d is the activation energy for diffusion, and R is the molar gas constant.

Supposing that the volume per atom is invariable, in terms of the lever rule of phase equilibria, the volume fraction at peak age (f_m) is as follows [33]:

$$f_m=\frac{C_0-C_e}{C_p-C_e} \tag{5}$$

The precipitation kinetics of artificial aging follows the Johnson−Mehl, Avrami, Kolmogorov (JMAK) models [34]:

$$f_v=f_m[1-\exp(-kt^n)] \tag{6}$$

where f_v is the volume fraction of precipitates, n is the Avrami index depending on the reaction mechanism, and k is the time constant related to with the nucleation rate and growth rate.

$$k = k_0 \exp[-Q_A/(RT)] \tag{7}$$

where k_0 is the pre-exponential constant, and Q_A is the equivalent activation energy. The variation in the number density, N_v, is described as a function of time [34]:

$$N_v = \frac{f_v}{\pi r^2 l} \tag{8}$$

3.2 Strength description

The equation of Vickers hardness H_v and yield strength σ_y can be written as [35,36]:

$$H_v = 0.33\sigma_y + 16 \tag{9}$$

Supposing that diverse strengthening factors to the overall strength satisfy the relationship of linear addition, the yield strength can be given by [35,36]

$$\sigma_y = \sigma_0 + \Delta\sigma_{ss} + \Delta\sigma_p \tag{10}$$

where σ_0 is the yield strength of pure aluminum with 10 MPa, and $\Delta\sigma_{ss}$ is the strengthening term of solid solution, given by [36]:

$$\Delta\sigma_{ss} = \sum\left(k_j C_j^{2/3}\right) \tag{11}$$

where k_j is the relevant scaling factor, and C_j is the concentration of a given alloying element in a solid solution. The increment of yield strength $\Delta\sigma_p$ of precipitation strengthening with Ashby−Orowan model can be expressed as [37]

$$\Delta\sigma_p = 0.538Gb\sqrt{f_v}\ln(\bar{R}/b)/(2\bar{R}) \tag{12}$$

where G represents the shear modulus, b is the amplitude of the Burgers vector, and $\bar{R}$ is the average radius of precipitates.

Supposing that all precipitates are cylindrical with aspect ratio A_1=4, 10, all input parameters applied in the microstructure and strength models are listed in Tables 1 and 2, respectively.

Table 1 Summary of input data used in microstructure model

Parameter	Value	Comment	Source
C_0/wt.%	1.01	Mg content in matrix	This work
C_e/wt.%	0.306	Equilibrium Mg content at interface	This work
C_p/wt.%	41.7	Mg content in Mg_5Si_6	This work
D_0/(m^2·s^{-1})	2.2×10^{-4}	Pre-exponential term for D	[36]
D/(m^2·s^{-1})	1.529×10^{-19}	Diffusion coefficient	This work
Q_d/(kJ·mol^{-1})	130	Activation energy for diffusion	[36]
Q_A/(kJ·mol^{-1})	152618	Equivalent activation energy	[33]
k	1.107×10^{-5}	Time constant	[36]
k_0	6.907×10^{12}	Pre-exponential term constant	[33]
R/(J·mol^{-1}·K^{-1})	8.314	Molar gas constant	[33]
n	1.25	Avrami index	This work

Table 2 Summary of input data used in strength model

Parameter	Value	Comment	Source
f_m/%	1.688	Volume fraction at peak age	This work
G/Pa	2.7×10^{10}	The magnitude of shear modulus	[33]
b/m	2.84×10^{-10}	The magnitude of the Burgers vector	[33]
σ_0/MPa	10	Intrinsic stress	[38]
k_{Mg}/(MPa·wt.%$^{-2/3}$)	29	Solid solution parameter for Mg	[36]
k_{Si}/(MPa·wt.%$^{-2/3}$)	66.3	Solid solution parameter for Si	[36]

4 Results and discussion

4.1 Precipitate characterization by SAXS

The temporal evolution of the SAXS curves of Al−Mg−Si alloy from as-quenching to artificial aging for 9 h is shown in Fig. 2(a). The power-law decreasing in the low-q region of 0.1−0.3 nm^{-1} (q is the amplitude of scattering vector, denoted by $q=4\pi\sin(\theta/2)/\lambda$, where θ is scattering angle and λ is X-ray wavelength) is associated with the asymptotic scattering behavior of micrometer-scale cluster particles. The nearly coincident SAXS curves in the low-q region indicate that large particles maintain constant volume during artificial aging. Besides, the change of the scattering intensity in the intermediate q region (0.3−0.8 nm^{-1}) is primarily attributed to the nucleation and growth of the GP zones and β'' precipitates. From 1 to 5 h aging, SAXS intensities in the intermediate q region increase with the increase of aging time, implying the nucleation and growth of β'' precipitates. Moreover, the SAXS curves collected for 7 and 9 h are almost identical in the intermediate q region, showing coarsening emergence of β'' precipitates. The SAXS curves in Fig. 2(a) can be described below due to the concurrence of precipitates and clusters during precipitation:

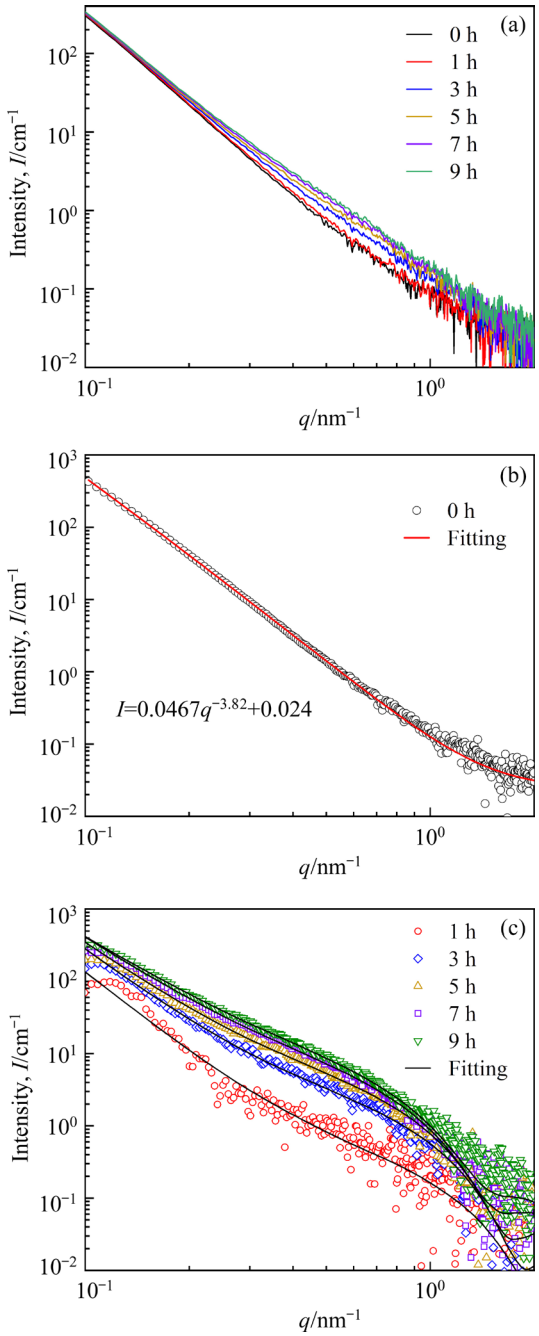

Fig. 2 Radial scattering intensity (I) as function of amplitude of scattering vector (q): (a) Temporal SAXS curves illustrating recorded data for six aging time; (b) Simulated SAXS curve for 0 h aging with fitting result; (c) SAXS plots simulated with rod-like precipitates and evolving cluster scattering of 6082 alloys aged at 175 °C with aging time

$$I(q)=I_{\text{precip}}(q)+BI_{\text{clutster}}(q,t_0)+C \tag{13}$$

$$I_{\text{clutster}}(q,t_0)=0.0467q^{-3.82}+0.024 \tag{14}$$

where $I_{\text{precip}}(q)$ is the scattering contribution of the rod-like β'' precipitates. B is the percentage of the surviving or non-dissolved clusters during artificial aging. $I_{\text{cluster}}(q,t_0)$ represents the SAXS profile measured at room temperature (RT) corresponding to the scattering contribution of all initial clusters. C is a constant incoherent background. $I_{\text{cluster}}(q,t_0)$ can be fitted using the scattering at 0 h and RT before heating and results in $I_{\text{cluster}}(q,t_0)=0.0467q^{-3.82}+0.024$, as shown in Fig. 2(b). The rod-like particle scattering $I_{\text{precip}}(q)$ can be expressed as

$$I_{\text{precip}}(q)=I_{\text{precip}}(0)P(q)=f_{\text{v}}(\Delta\rho)^2V_{\text{P}}P(q) \tag{15}$$

$$P(q)=\int_0^{\pi/2}\left(\frac{\sin(0.5ql\cos\varphi)}{0.5ql\cos\varphi}\right)^2\cdot\left(\frac{2J_1(qr\sin\varphi)}{qr\sin\varphi}\right)^2\sin\varphi\mathrm{d}\varphi \tag{16}$$

where $I_{\text{precip}}(0)$ is the $I_{\text{precip}}(q)$ at q=0. $P(q)$ is the normalized form factor for cylindrical precipitates [15]. $\Delta\rho$ is the scattering length density contrast between the β'' precipitates and Al matrix, V_{P} is the volume of a cylindrical particle with radius

r and length l, J_1 is the first-order Bessel function, and φ is the angle between the axis of the cylinder.

In terms of $I_{precip}(q)$ curves in Fig. 2(c), the simulated structural parameters are thus extracted by the model fitting, as summarized in Table 3. The radius and length from the SAXS simulation of Eq. (13) are (2.2±0.4) nm and (20±8) nm, respectively, which are similar to those achieved from SAXS analysis [14,15] and TEM studies [8,9]. The length of β'' precipitates increases from 13 nm at 0 h to 28 nm at 9 h and presents a continuously growing trend. Note that temporal and structural evolutions of β'' precipitates show a tardy radius and a rapidly increasing length with aging time. Overall, the structural evolutions of β'' precipitates in size, volume fraction, and number density from 1 to 9 h aging can be featured by the representative nucleation, growth, and coarsening stage.

4.2 Precipitate observation by TEM

The bright-field TEM micrographs and high-resolution images with fast Fourier transformation (FFT) images with different aging time are shown in Fig. 3. After aging for 1 h, fine grey spot-like precipitates with a diameter of 2−4 nm are observed in Fig. 3(a) and identified from the high-resolution

Table 3 Summary of structural parameters identified by model simulation

Time/h	$B/10^{-2}$	β	r/nm	l/nm	V_p/nm^3	$I_{precip}(0)$/cm^{-1}	f_v/%	$N_v/10^{16}$ cm^{-3}
1	0.2493	3.73	1.8	13	132.3	0.1294	0.33	2.47
3	0.7686	3.55	2.1	24	332.3	1.0631	1.07	3.22
5	1.413	3.36	2.3	27	448.5	1.9599	1.46	3.26
7	2.514	3.18	2.5	28	549.5	2.7136	1.65	3.00
9	3.864	3.00	2.6	28	594.3	3.1328	1.76	2.96

$I_{precip}(0)$ is the $I_{precip}(q)$ at the lower limit of detectable value q=0.09 nm^{-1}. $\Delta\rho$=−1.73×10^{10} cm^{-2} between β'' precipitates (Mg_5Si_6) and pure α(Al). $N_v=f_v/V_p=f_v/(\pi r^2 l)$

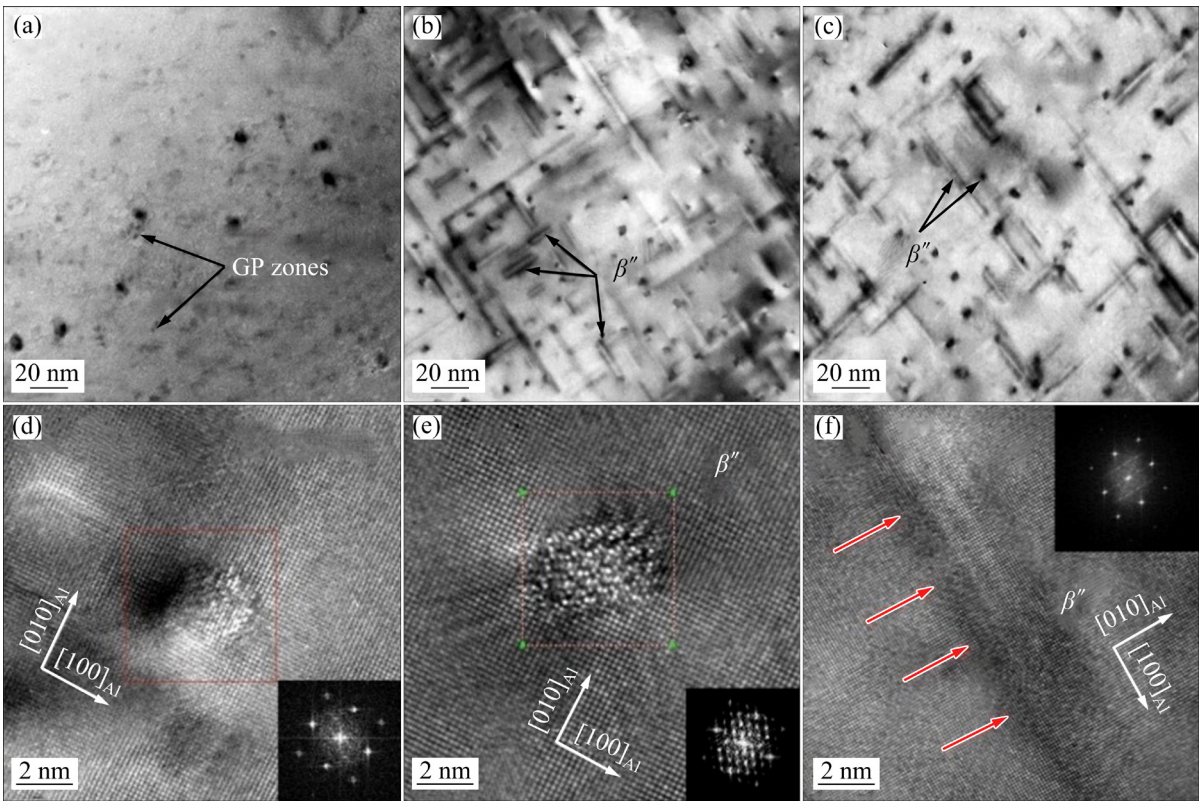

Fig. 3 Bright-field TEM images of precipitates oriented along $[001]_{Al}$ zone axis (a−c), and high-resolution TEM images and corresponding fast Fourier transforms (FFT) patterns of typical precipitates at 175 °C for different aging time (d−f): (a, d) 1 h; (b, e) 5 h; (c, f) 9 h

image in Fig. 3(d). It is indicated that precipitates have a similar crystallographic structure and lattice orientation as the matrix, which can be recognized as GP zones, as reported by MURAYAMA et al [39].

The peak-aged microstructure (aging for 5 h) is exhibited in Fig. 3(b) and needle-like and spot-like precipitates are displayed. The needle-like precipitates with lengths align to $[001]_{Al}$ directions belong to the monoclinic system, as seen in Fig. 3(e). They can be identified as β'' precipitates according to their morphology, orientation and crystal structure. In addition, the spot-like precipitates with a diameter of about 2.8 nm are the cross-sections of needle-like β'' precipitates. The cross-section presents distortion in lattice fringes and this implies incoherency with the matrix, as depicted in Fig. 3(e). Therefore, it is verified that most GP zones are transformed into β'' precipitates at aging time from 1 to 5 h.

Figure 3(c) shows the TEM bright-field micrograph aged for 9 h at 175 °C. It can be seen that β'' precipitates still dominate and grow further in the axial and radial directions. The number of GP zones and fine particles decreases while large precipitates grow during the aging process. Moreover, the average radius and mean length of precipitates increase from (2.4±0.18) nm in 1 h to (3.3±0.18) nm in 9 h and from (8±1.3) nm in 1 h to (27±1.25) nm in 9 h, respectively. Summarily, the size and morphology of precipitates change with the increasing aging time.

4.3 Temporal evolution of microstructural parameters

The temporal evolution of the mean radius and mean length of β'' precipitates using SAXS measured values compared with predicted lines is shown in Figs. 4(a, b). As can be seen, a gradual increase in radius and length of precipitates at aging time from 1 to 5 h indicates classic nucleation and growth behavior from supersaturated solid solution. After 5 h, the radius evolution of β'' precipitates changes with typical early-stage coarsening behavior. Furthermore, tardive growth

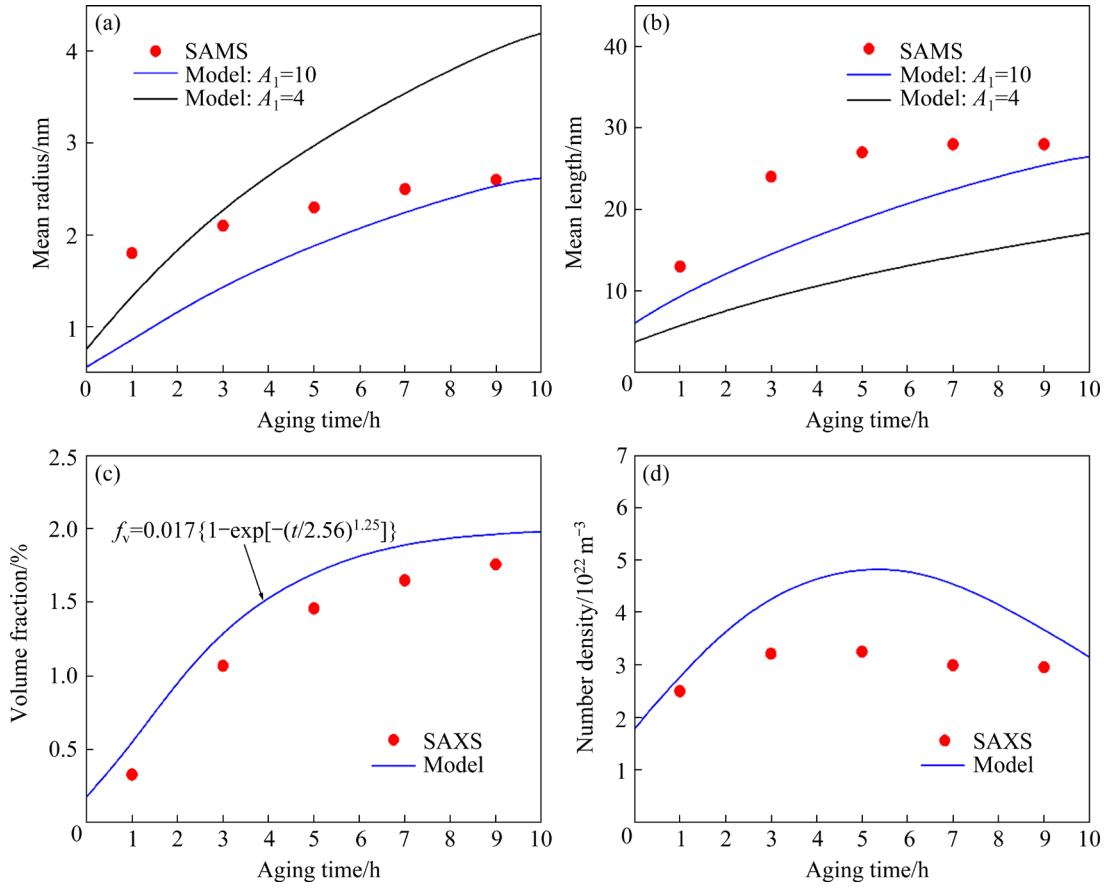

Fig. 4 Effect of isothermal aging time on precipitate properties: (a, b) Mean radius and mean length obtained from SAXS data and model fitting, respectively; (c, d) Volume fraction and number density identified from SAXS data and microstructure model prediction, respectively

rate of radius and rapid increasing length represent that interface diffusion controls precipitates growth. These growth features can reasonably interpret the transition from spherical clusters to rod-like precipitates, which sustain the unchanged radius of clusters generated at the nucleation stage of precipitation. It is worth noting that the results of mean radius and length using the model-fitting method are consistent with the results of the microstructure model in Figs. 4(a, b).

As shown in Figs. 4(c, d), the first stage (up to about 3 h) is associated with the nucleation of β'' precipitates due to the growing number density of β'' precipitates. Then, the typical growth (from 1 to 5 h) stage occurs until the depletion of the Mg and Si elements in the matrix. Subsequently, β'' precipitate undergoes Ostwald ripening after 5 h because of the decline of number density of β'' precipitate. It can also be found in Fig. 4(a) that the mean radius results of SAXS in 1 and 3 h are close to those of the model for A=4, the average radius values of SAXS in 5 and 9 h approach those of model for A_1=10. It is indicated that the aspect ratio changes with the growth of aging time, and the model with a constant aspect ratio cannot accurately predict the radius variation of the β'' precipitates. This finding agrees with that of the study of BAHRAMI et al [33]. Thus, the growth rate of longitudinal precipitates is higher than that of radial ones, indicating that the growth of precipitates is interface-reaction dominant.

Figure 4(c) shows the temporal volume fraction evolution of β'' precipitates with the aging process using SAXS measurement and model prediction. It can be seen that the volume fraction change of β'' precipitate follows the JMAK equation. Due to the relatively slow precipitation rate of solute atoms, the volume fraction of β'' precipitate continues to increase after aging for 5 h, indicating that the stable equilibrium state has not been reached. Moreover, the model presents faster-aging dynamics in the underaged stage compared with the aging dynamics from SAXS. It is possibly owing to the hypothesis of incubation time being zero. The higher volume fraction of the precipitate obtained by the model is attributed to the assumption that all Si atoms are involved in precipitation. Some Si atoms are partitioned into Fe and Mn-containing particles [33].

The number density of β'' precipitates firstly increases from 1 to 5 h and then decreases after 5 h aging (Fig. 4(d)), resulting in a decrease and then an increase in mean distance between precipitates. In addition, the lower number density of the precipitates also contributes to a larger mean radius at peak aging. The evolution of the precipitate radius is approximately linear with aging time. The length and volume fraction of precipitates are observed to enhance rapidly (up to about 5 h of aging) and then level off. In contrast, the number density of precipitate increases rapidly and then decreases slowly. Eventually, this evolution indicates a first stage (before 5 h aging) of nucleation and growth at an almost invariable radius, followed by a stage of precipitate coarsening.

The number density discrepancy between SAXS and the model is probably due to the growth of particle and matrix interfacial energy during the formation of incoherent precipitates, which cannot be interpreted using simulation. The first stage (before 3 h) is associated with the nucleation of precipitates due to the growing number density of precipitates. Then, the typical growth (from 1 to 5 h) stage occurs until the depletion of Mg and Si elements in the matrix and subsequently, precipitates undergo Ostwald ripening after 5 h, because of the declining number density of precipitates. Finally, the temporal evolution of volume fraction and number density of precipitates provides a basic understanding of precipitation kinetics.

4.4 Temporal evolution of mechanical properties

The measured stress−strain curves of the Al−Mg−Si alloy aged at 175 °C for different time are shown in Fig. 5. The yield strength, tensile strength and elongation of the specimens are summarized in Table 4. Increasing the aging time from 1 to 5 h significantly improves the yield strength from 250.3 to 331.9 MPa, respectively. At an aging time of 7 h, the yield strength value reaches its maximum of 336.8 MPa. When the specimen is aged for a longer time of 9 h, which is an over-aged state, the yield strength decreases to 329.1 MPa. It is found that the strength variation in terms of the yield strength has the highest value at the corresponding peak aging time. Consequently, while the yield strength exhibits a similar trend to

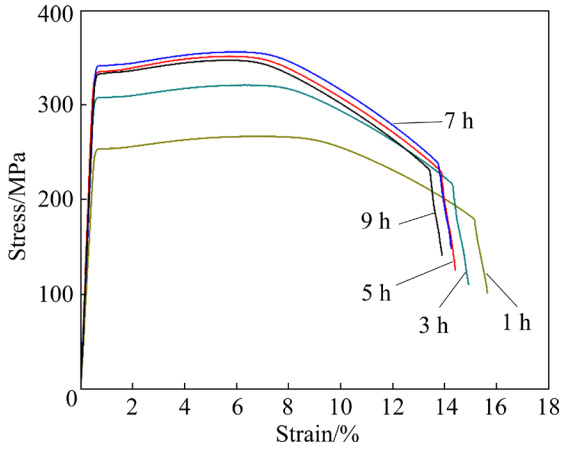

Fig. 5 Stress−strain curves of Al−Mg−Si alloy aged at 175 °C for different time

Table 4 Tensile test results of Al−Mg−Si alloy aged at 175 °C for different time

Aging time/h	Yield strength/MPa	Tensile strength/MPa	Elongation/%
1	250.3	267.5	15.2
3	294.4	318.7	14.4
5	331.9	348.2	13.9
7	336.8	350.8	13.7
9	329.1	345.6	13.3

the tensile strength during aging at 175 °C, the elongation decreases with increasing aging time from 1 to 9 h.

Figure 6(a) presents the measured and predicted yield strength results from SAXS and the microstructure model of Al−Mg−Si alloy. The yield strength results of Al−Mg−Si alloy aged for different aging time are shown in Table 5. It is observed that the predicted values from SAXS are in broadly good agreement with the actual counterparts except for underestimation at 1 h aging time. Nevertheless, the results from the microstructure model overestimate yield strength for the whole aging process. This overestimation of yield strength is related to the overvaluation volume fraction of precipitates in the model, resulting from the assumption that all Si atoms are involved in precipitation. In addition, the discrepancy of yield strength and hardness between experiment and model prediction is attributed to model calculation depending on circular cross-sections, which cannot represent the shape of precipitates with anisotropic strain fields [40]. The difference between the model

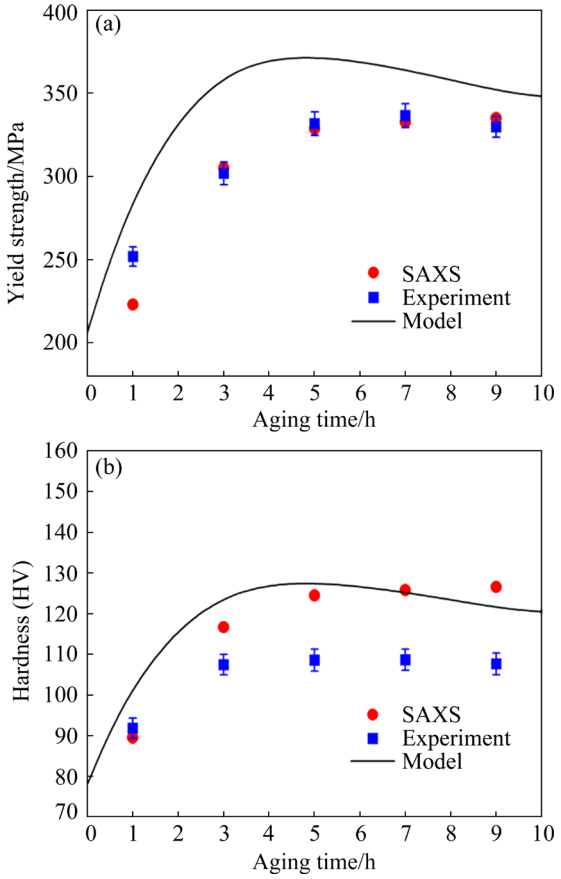

Fig. 6 Effect of isothermal aging time on measured and calculated yield strength (a) and hardness (b)

Table 5 Yield strength results of Al−Mg−Si alloy aged for different time

Aging time/h	Yield strength/MPa		
	Experiment	SAXS	Model
1	250.3	223.1	294.7
3	294.4	305.3	353.6
5	331.9	328.8	374.3
7	336.8	332.7	362.4
9	329.1	335.3	351.2

and experiment can be associated with a transformation in the precipitate−dislocation interaction mechanism [15]. The interaction and edge effects between precipitates and strain fields should be contained in the model to raise predictive power. Therefore, the prediction from SAXS is closer to the experiment, which indicates that structural parameters obtained by SAXS have higher reliability.

Figure 6(b) shows the measured and predicted hardness from SAXS and the microstructure model

of Al−Mg−Si alloy. The hardness results of Al−Mg−Si alloy aged for different aging time are shown in Table 6. It should be noted that the predicted hardness result from SAXS is almost consistent with the experimental and model values at aging time of 1 h. After 3 h aging the hardness result from SAXS gradually deviates from the experimental value and approaches the micro-structure model value since model calculation depends on circular cross-sections, which cannot represent the real shape of β'' precipitates with anisotropic strain fields [41]. It indicates no simple linear relationship between the microhardness and Eq. (9) that needs to be corrected and further researched. The hardness of alloy aged for 5 h is higher than that aged for 1 and 3 h. However, there is a significant decline in hardness after 7 h aging, indicating a distinct decrease in resistance to dislocation movement [15]. Thus, the data of the mechanical properties obtained by SAXS are closer to the experimental results than the aging strengthening model, which indicates that the structural parameters obtained by SAXS have higher reliability.

Table 6 Hardness results of Al−Mg−Si alloy aged for different aging time

Aging time/h	Hardness (HV)		
	Experiment	SAXS	Model
1	91.9	89.6	104.4
3	107.5	116.7	124.8
5	108.6	124.5	127.5
7	108.7	125.8	125.2
9	107.7	126.6	121.3

When the coherent interfaces emerge between the β'' precipitates and the matrix in the underaged stage, larger precipitates and strain fields can be induced by the coherent precipitates, thus hindering the dislocation motion because of the interaction between the strain field and the dislocation [41]. The radius growth of the β'' precipitates during the aging improves the ambient strain fields, making dislocation cutting through the precipitates more difficult and alloy strengthened. When the β'' precipitate size surpasses a critical value, the incoherent interface occurs in the overaged stage from 5 to 9 h aging, dislocation shearing through the precipitate becomes difficult, resulting in the reduction of the coherence. Additionally, the space between precipitates decreases during coarsening, which induces Orowan looping to emerge more efficiently, transitioning from dislocation shearing to Orowan looping. With the growth and coarsening of β'' precipitates, the shearable precipitates change into non-shearable precipitates and weaken the pinning effect of precipitates on dislocations. In contrast, small precipitates dissolve, resulting in further decline of the pinning effect of precipitates and a decrease in mechanical properties.

Some correlations can be found when comparing the mean radius and volume fraction of precipitates and predicted properties achieved by SAXS. Based on Fig. 6, Figs. 7(a, b) present yield strength and hardness curves with different aging time versus the mean radius and volume fraction of precipitates, respectively. It is important to note that the increase in yield strength and hardness at aging time from 1 to 5 h is directly influenced by the growing volume fraction of precipitates, which outweighs the enhancing radius of precipitates.

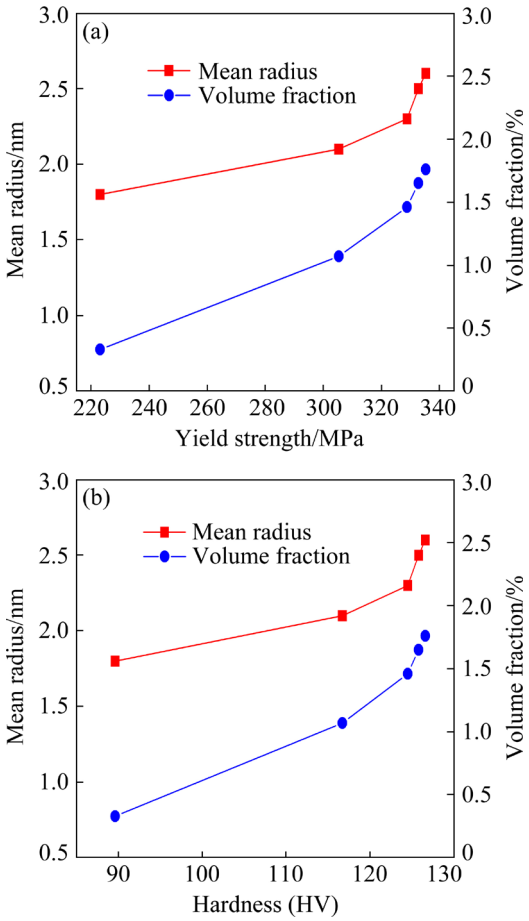

Fig. 7 Curves for yield strength (a) and hardness (b) versus mean radius and volume fraction of precipitates

Nevertheless, compared with that of 5 and 7 h aging, there are larger precipitate radius and volume fraction of 9 h aging, but their mechanical properties are comparable, ascribing to micro-structure and precipitates of 9 h aging similar to those of 5 and 7 h aging. Subsequently, the growth of volume fraction is analogous to that of mean radius after 5 h aging, contributing to the inconspicuous increase in performance.

5 Conclusions

(1) The precipitation strengthening behavior of Al−Mg−Si alloy during artificial aging is investigated by the in-situ SAXS and Ashby−Orowan model. A modified algorithm can extract structural parameters (size, volume fraction and number density) of β'' precipitates (Mg_5Si_6).

(2) The growth rate of longitudinal dimensions is larger than that of radial dimensions, implying that interface diffusion controls the precipitate growth. The volume fraction of precipitates measured by SAXS is consistent with the value predicted by the microstructure model.

(3) The yield strength predicted by the Ashby−Orowan model with structural parameters from SAXS is more consistent with the experimental values than that obtained by the microstructure model, based on more reliable input data from SAXS. The excellent ability to predict mechanical properties can provide technical support for selecting heat treatment processing schedules in actual production.

Acknowledgments

The authors gratefully acknowledge the financial supports from the National Natural Science Foundation of China (Nos. 51627802, 51504150, 11875192), the National Key Research and Development Program of China (No. 2020YFB0311200), and the Shanghai Science and Technology Committee, China (No.16DZ2260602). The staff of the BL16B1 beamline, SSRF, is thanked for technical help.

References

[1] GRANUM H, MYHR O R, BØRVIK T, HOPPERSTAD O S. Effect of pre-stretching on the mechanical behaviour of three artificially aged 6xxx series aluminium alloys [J]. Materials Today Communications, 2021, 27(7): 102408.

[2] ZHANG Qun-li, LUAN Xi, DHAWAN S, POLITIS D J, DU Qiang, FU Ming-wang, WANG Ke-huan, GHARBI M M, WANG Li-liang. Development of the post-form strength prediction model for a high-strength 6xxx aluminium alloy with pre-existing precipitates and residual dislocations [J]. International Journal of Plasticity, 2019, 119: 230−248.

[3] YANG Ming-jun, OREKHOV A, HU Zhi-yi, FENG Man, JIN Shen-bao, SHA Gang, LI Kai, SAMAEE V, SONG Min, DU Yong, TENDELOO G V, SCHRYVERS D. Shearing and rotation of β'' and β' precipitates in an Al−Mg−Si alloy under tensile deformation: In-situ and ex-situ studies [J]. Acta Materialia, 2021, 220: 117310.

[4] GIOFRE D, JUNGE T, CURTIN W A, CERIOTTI M. Ab initio modelling of the early stages of precipitation in Al-6000 alloys [J]. Acta Materialia, 2017, 140: 240−249.

[5] GAO Guan-jun, HE Chen, LI Yong, LI Jia-dong, WANG Zhao-dong, MISRA R D K. Influence of different solution methods on microstructure, precipitation behavior and mechanical properties of Al−Mg−Si alloy [J]. Transactions of Nonferrous Metals Society of China, 2018, 28: 839−847.

[6] WANG Guang-dong, TIAN Ni, CAO Jing-yi, ZHOU Yi-ran, ZHAO Gang, ZUO Liang. Yield strength prediction of rolled Al−(1.44−12.40)Si−0.7Mg alloy sheets under T4 condition [J]. Transactions of Nonferrous Metals Society of China, 2020, 30(8): 2045−2055.

[7] MAEDA T, KANEKO K, NAMBA T, KOSHINO Y, SATO Y, TERANISHI R, ARUGA Y. Structural and compositional study of precipitates in under-aged Cu-added Al−Mg−Si alloy [J]. Scientific Reports, 2018, 8(1): 1−7.

[8] CHROMINSKI W, LEWANDOWSKA M. Precipitation phenomena in ultrafine grained Al−Mg−Si alloy with heterogeneous microstructure [J]. Acta Materialia, 2016, 103: 547−557.

[9] HUA Lin, YUAN Pu-guang, ZHAO Ning, HU Zhi-li, MA Hui-juan. Microstructure and mechanical properties of 6082 aluminum alloy processed by preaging and hot forging [J]. Transactions of Nonferrous Metals Society of China, 2022, 32(3): 790−800.

[10] BUCHANAN K, COLAS K, RIBIS J, LOPEZ A, GARNIER J. Analysis of the metastable precipitates in peak-hardness aged Al−Mg−Si(−Cu) alloys with differing Si contents [J]. Acta Materialia, 2017, 132: 209−221.

[11] ZANDBERGEN M W, XU Q, CEREZO A, SMITH G D W. Study of precipitation in Al−Mg−Si alloys by Atom Probe Tomography I. Microstructural changes as a function of ageing temperature [J]. Acta Materialia, 2015, 101: 136−148.

[12] ZANDBERGEN M W, CEREZO A, SMITH G D W. Study of precipitation in Al−Mg−Si Alloys by atom probe tomography. II: Influence of Cu additions [J]. Acta Materialia, 2015, 101: 149−158.

[13] ASHBY M F. Oxide dispersion strengthening [M]. New York: Gordon and Breach, 1968: 431−468.

[14] SHI Rong-jian, WANG Zi-dong, QIAO Li-jie, PANG Xiao-lu. Microstructure evolution of in-situ nanoparticles and its comprehensive effect on high strength steel [J]. Journal of Materials Science & Technology, 2019, 35(9): 1940−1950.

[15] WANG Y Q, CLARK S J, JANIK V, HEENAN R K, ALBA VENERO D, YAN K, MCCARTNEY D G, SRIDHAR S, LEE P D. Investigating nano-precipitation in a V-containing HSLA steel using small angle neutron scattering [J]. Acta Materialia, 2018, 145: 84−96.

[16] TANG Chao-lan, ZHOU De-jing. Precipitation hardening behavior of dilute binary Al−Yb alloy [J]. Transactions of Nonferrous Metals Society of China, 2014, 24(7): 2326−2330.

[17] LU F, SUNDE J K, MARIOARA C D, HOLMESTAD R, HOLMEDAL B. An improved modelling framework for strength and work hardening of precipitate strengthened Al−Mg−Si alloys [J]. Materials Science and Engineering A, 2022, 832: 142500.

[18] ZHU Lin, QIU Feng, ZOU Qian, HAN Xue, SHU Shi-li, YANG Hong-yu, JIANG Qi-chuan. Multiscale design of α-Al, eutectic silicon and Mg_2Si phases in Al−Si−Mg alloy manipulated by in situ nanosized crystals [J]. Materials Science and Engineering A, 2021, 802: 140627.

[19] BARNETT M R, WANG Huan, GUO Ting-ting. An Orowan precipitate strengthening equation for mechanical twinning in Mg [J]. International Journal of Plasticity, 2019, 112: 108−122.

[20] SUN W T, QIAO X G, ZHENG M Y, XU C, KAMADO S, ZHAO X J, CHEN H W, GAO N, STARINK M J. Altered ageing behaviour of a nanostructured Mg−8.2Gd−3.8Y−1.0Zn−0.4Zr alloy processed by high pressure torsion [J]. Acta Materialia, 2018, 151: 260−270.

[21] ELGALLAD E M, LIU K, ZHANG Z, CHEN X G. Effect of transition elements on dispersoid formation and elevated-temperature mechanical properties in 6082 aluminum alloy [J]. Philosophical Magazine, 2021, 101(1): 96−116.

[22] WANG Yi-chang, WU Xiao-dong, CAO Ling-fei, TONG Xin, ZOU Yan, ZHU Qian-qian, TANG Song-bai, SONG Hui, GUO Ming-xing. Effect of Ag on aging precipitation behavior and mechanical properties of aluminum alloy 7075 [J]. Materials Science and Engineering A, 2021, 804: 140515.

[23] LI Z, ZHANG Z, CHEN X G. Effect of magnesium on dispersoid strengthening of Al−Mn−Mg−Si (3xxx) alloys [J]. Transactions of Nonferrous Metals Society of China, 2016, 26(11): 2793−2799.

[24] IVANOV R, DESCHAMPS A, de GEUSER F. Clustering kinetics during natural ageing of Al−Cu based alloys with (Mg, Li) additions [J]. Acta Materialia, 2018, 157: 186−195.

[25] DESCHAMPS A, HUTCHINSON C R. Precipitation kinetics in metallic alloys: Experiments and modeling [J]. Acta Materialia, 2021, 220: 117338.

[26] SINGH M A, SAIMOTO S, LANGILLE M R, LEVESQUE J, INAL K, WOLL A R. Small-angle X-ray scattering investigation of deformation-induced nanovoids in AA6063 aluminium alloy [J]. Philosophical Magazine, 2017, 97(28): 2496−2513.

[27] BANHART J, YANG Zi, LIU Meng, MADANAT M, ZHANG Xin-pu, GUO Qian-ning, YAN Yong, RÖHSLER A, FRICKE K, LIANG Ze-qin, LEYVRAZ D, HOELL A, GERICKE E, WENDT R, LIU Chun-hui. Exploring the hidden world of solute atoms, clusters and vacancies in aluminium alloys [J]. MATEC Web of Conferences, 2020, 326: 01001.

[28] TSAO C S, CHEN C Y, JENG U S, KUO T Y. Precipitation kinetics and transformation of metastable phases in Al−Mg−Si alloys [J]. Acta Materialia, 2006, 54(17): 4621−4631.

[29] TSAO C S, JENG U S, CHEN C Y, KUO T Y. Small-angle X-ray scattering study of nanostructure evolution of β'' precipitates in Al−Mg−Si alloy [J]. Scripta Materialia, 2005, 53(11): 1241−1245.

[30] SITDIKOV V D, CHIZHOV P S, MURASHKIN M Y, VALIEV R Z. Simulation of small-angle X-ray scattering curves to determine the size, shape and distribution of secondary phases in dynamically aged aluminum alloy 6201 [J]. Reviews on Advanced Materials Science, 2016, 47(1/2): 59−65.

[31] LIU G, ZHANG G J, DING X D, SUN J, CHEN K H. Modeling the strengthening response to aging process of heat-treatable aluminum alloys containing plate/disc-or rod/needle-shaped precipitates [J]. Materials Science and Engineering A, 2003, 344(1/2): 113−124.

[32] FERRANTE M, DOHERTY R D. Influence of interfacial properties on the kinetics of precipitation and precipitate coarsening in aluminium−silver alloys [J]. Acta Metallurgica, 1979, 27(10): 1603−1614.

[33] BAHRAMI A, MIROUX A, SIETSMA J. An age-hardening model for Al−Mg−Si alloys considering needle-shaped precipitates [J]. Metallurgical and Materials Transactions A, 2012, 43(11): 4445−4453.

[34] NIE J F, MUDDLE B C. Microstructural design of high-strength aluminum alloys [J]. Journal of Phase Equilibria, 1998, 19(6): 543−551.

[35] MYHR O R, GRONG Ø. Modelling of non-isothermal transformations in alloys containing a particle distribution [J]. Acta Materialia, 2000, 48(7): 1605−1615.

[36] MYHR O R, GRONG Ø, ANDERSEN S J. Modelling of the age hardening behaviour of Al−Mg−Si alloys [J]. Acta Materialia, 2001, 49(1): 65−75.

[37] KAMIKAWA N, ABE Y, MIYAMOTO G, FUNAKAWA Y, FURUHARA T. Tensile behavior of Ti, Mo-added low carbon steels with interphase precipitation [J]. ISIJ International, 2014, 54(1): 212−221.

[38] DESCHAMPS A, BRECHET Y. Influence of predeformation and ageing of an Al−Zn−Mg alloy. II: Modeling of precipitation kinetics and yield stress [J]. Acta Materialia, 1998, 47(1): 293−305.

[39] MURAYAMA M, HONO K, MIAO W F, LAUGHLIN D E. The effect of Cu additions on the precipitation kinetics in an Al−Mg−Si alloy with excess Si [J]. Metallurgical and Materials Transactions A, 2001, 32(2): 239−246.

[40] NINIVE P H, STRANDLIE A, GULBRANDSEN-DAHL S, LEFEBVRE W, MARIOARA C D, ANDERSEN S J, FRIIS J, HOLMESTAD R, LØVVIK O M. Detailed atomistic insight into the β'' phase in Al−Mg−Si alloys [J]. Acta Materialia, 2014, 69: 126−134.

[41] SMALLMAN R E, BISHOP R J. Modern physical metallurgy and materials engineering [M]. 6th ed. Oxford: Butterworth-Heinemann, 1999.

采用同步辐射小角 X 射线散射技术研究 Al−Mg−Si 合金的析出强化行为

刘 涛[1,2,3]，胡光敏[1]，王玉杰[1]，曾建荣[2,3]，东 青[1]，
边风刚[2,3]，曹召鹏[2,3]，孟 楠[2,3]，张 佼[1,4,5]，孙宝德[1,4,5]

1. 上海交通大学 材料科学与工程学院 上海市先进高温材料与精密成形重点实验室，上海 200240；
2. 中国科学院 上海高等研究院，上海 201204；
3. 中国科学院 上海应用物理研究所，上海 201800；
4. 上海交通大学 金属基复合材料国家重点实验室，上海 200240；
5. 上海交通大学 先进船舶与深海探测协同创新中心，上海 200240

摘 要：研究 Al−Mg−Si 合金在等温时效过程中的析出强化行为及其对力学性能的影响。利用原位同步辐射小角 X 射线散射(SAXS)技术和透射电子显微镜(TEM)对纳米析出相及其结构参数(尺寸、体积分数和数密度)进行表征。结果表明，棒状 β''析出相优先沿其纵向尺寸生长，但径向尺寸在时效 5 h 后达到峰值。如预测与测量的屈服强度和硬度结果所示，纳米析出相的尺寸和体积分数的增大与析出强化定量相关。SAXS 为 Ashby−Orowan 模型提供了更可靠的输入参数，这有助于提高模型的预测精度和泛化能力。研究表明，随着时效时间的延长，Al−Mg−Si 合金预测力学性能的演变与 β''析出相的平均半径和体积分数有关。

关键词：析出行为；Al−Mg−Si 合金；小角 X 射线散射；力学性能

(Edited by Wei-ping CHEN)